Coupled amplitude-phase transport in heterogeneous optical media

Masaki Watabe,[1,2,*,†] Joe Sakamoto,[3,4,*] Hideaki Yoshimura,[5] Tomomi Nemoto,[3,4] and Kazunari Kaizu[1,6]

[1]*Cell Modeling and Simulation Research Group, The Exploratory Research Center on Life and Living Systems, Okazaki, Aichi 444-8787, Japan*

[2]*Interdisciplinary Research Unit, National Institute for Basic Biology, Okazaki, Aichi 444-8585, Japan*

[3]*Biophotonics Research Group, The Exploratory Research Center on Life and Living Systems, Okazaki, Aichi 444-8787, Japan*

[4]*Division of Biophotonics, National Institute for Physiological Sciences, Okazaki, Aichi 444-8585, Japan*

[5]*School of Science, The University of Tokyo, 7-3-1 Hongo, Bunkyo-ku, Tokyo 113-0033, Japan*

[6]*Laboratory for Biologically Inspired Computing, RIKEN Center for Biosystems Dynamics Research, Kobe, Hyogo 650-0047, Japan*

(Received 17 June 2025; accepted 1 May 2026; published 18 May 2026)

The transport of intensity equation (TIE) enables deterministic phase retrieval in optical microscopy, yet its application to heterogeneous media exhibiting both refractive-index variations and attenuation remains an open problem. We derive a coupled TIE-TPE (transport of phase equation) framework from the paraxial wave equation with a complex optical potential, in which the refractive index field is decomposed into a spatially uniform mean field and a local fluctuation field through Reynolds decomposition. This formulation yields a nondivergent system of transport equations that simultaneously reconstructs refractive-index fluctuations and attenuation coefficients within the condition $|\Delta n| < 1$, without requiring linearization or weak-absorption approximations. We establish explicit validity bounds that define the measurable parameter space for a given experimental configuration, emerging from both photon counting statistics and the diffraction limit. Experimental validation using microlens arrays and HeLa cells demonstrates robust recovery of optical properties, including in the transparent-limit regime where attenuation signals approach detection thresholds. We further verify that the attenuation asymmetry parameter remains consistent with zero across three orders of magnitude in optical depth, indicating preservation of optical reciprocity in structurally heterogeneous biological media.

DOI: 10.1103/zjh7-3bdb

I. INTRODUCTION

The transport of intensity equation (TIE), introduced by Teague in 1983 [1,2], provides a deterministic solution to the phase retrieval problem by relating phase gradients to axial intensity variations. This noninterferometric approach has become essential for label-free imaging of biological specimens [3–5], enabling quantitative measurement of cellular dry mass, protein concentration, and organelle structures. Because TIE requires only through-focus intensity images without reference beams or interferometric setups, it is particularly well suited to integration with standard microscopy platforms and has been widely adopted in biomedical and materials science applications.

However, the conventional TIE formulation assumes purely refractive objects—a condition that becomes invalid for real biological samples exhibiting both refractive-index variations and attenuation from scattering and absorption. When amplitude changes are present, the standard TIE no longer captures the full physics of wave propagation, since the imaginary part of the optical potential couples amplitude and phase evolution in a manner that cannot be separated by a single transport equation. This limitation has motivated several approaches to extend phase retrieval beyond the pure-phase regime.

One such direction is transport of intensity diffraction tomography (TIDT) [6,7], which extends TIE to three-dimensional reconstruction under the first Born approximation—valid only for weakly scattering samples. Within this framework, Bai *et al.* [8] demonstrated absorption-phase decoupling using multiple illumination apertures based on Wolf's scattering potential theory [9]. Their work showed that the refractive-index and absorption components of the scattered field can be separated through complementary transfer functions obtained under circular and annular illumination. However, this approach operates within the Born approximation, which inherently restricts applicability to weakly scattering samples, and the validity domains for experimental parameters—including defocus distance, numerical aperture, and sample optical properties—remain implicit in those approximations rather than explicitly established.

A more fundamental question, largely unaddressed in the existing literature, concerns the structure of the transport equations themselves when both refraction and attenuation

*These authors contributed equally to this work.
†Contact author: m-watabe@nibb.ac.jp

Published by the American Physical Society under the terms of the Creative Commons Attribution 4.0 International license. Further distribution of this work must maintain attribution to the author(s) and the published article's title, journal citation, and DOI.

are present. The paraxial wave equation with a complex optical potential yields, upon separation into real and imaginary parts, not one but two coupled transport equations: the generalized TIE governing intensity evolution and a transport of phase equation (TPE) governing phase evolution. While this mathematical structure follows from the paraxial approximation, extracting a physically consistent and nondivergent reconstruction framework from these equations is not straightforward. The challenge lies in formulating the coupled system so that both refractive-index fluctuations and attenuation coefficients can be simultaneously recovered with well-defined convergence properties and explicit validity conditions.

In this paper, we address this challenge by deriving a coupled TIE-TPE framework from the paraxial wave equation with complex optical potential, in which the refractive index field is decomposed into a spatially uniform mean field and a local fluctuation field through Reynolds decomposition. This formulation ensures mathematical convergence when the fluctuation field satisfies $|\Delta n| < 1$, yielding a nondivergent system that simultaneously reconstructs refractive-index fluctuations and attenuation coefficients without requiring linearization or weak-absorption approximations. We establish explicit reconstruction validity bounds—arising from both photon counting statistics and the diffraction limit—that define the measurable parameter space for a given experimental configuration.

We validate this framework through quantitative phase imaging of microlens arrays and living HeLa cells, demonstrating robust recovery of optical properties including in the transparent-limit regime where attenuation signals approach detection thresholds. Through this validation, we find that the attenuation asymmetry parameter $\mathcal{A}_\kappa$—quantifying the balance between forward and backward propagation modes—remains consistent with zero across three orders of magnitude in optical depth, confirming that optical reciprocity [10] is preserved in structurally heterogeneous biological media.

II. THEORETICAL FRAMEWORK

Light propagation through heterogeneous media involves complex interactions between electromagnetic waves and spatial variations in optical properties. To capture these physics systematically, we introduce a complex optical potential that accounts for both real and imaginary components of the refractive index field. The key insight is to express the spatially varying refractive index field as the product of a uniform mean field n_0 and a dimensionless function: $n(\mathbf{r}_\perp, z) = n_0[1 + \Delta n(\mathbf{r}_\perp, z)]$, where n_0 represents the mean field of the refractive index and $\Delta n(\mathbf{r}_\perp, z)$ is the fluctuation field capturing local deviations from this mean. This decomposition naturally separates the bulk optical properties from structural heterogeneities, allowing us to treat the fluctuation field Δn as a small parameter when $|\Delta n| < 1$. This decomposition is analogous to the Reynolds decomposition used in turbulence theory, where a field is separated into its spatial mean and local fluctuations.

Starting from the Helmholtz equation and applying the paraxial approximation, the wave equation becomes

$$i\frac{\partial A}{\partial z} = \left[-\frac{1}{2kn_0}\nabla_\perp^2 - \frac{\partial}{\partial z}(\beta + i\alpha)\right]A. \tag{1}$$

Here $A(\mathbf{r}_\perp, z)$ is the complex amplitude of the wave field, $kn_0 = 2\pi n_0/\lambda$ is the wave number in the mean medium, and $\nabla_\perp^2$ is the transverse Laplacian. The complex optical potential is encoded in two functions: $\alpha(r_\perp, z)$ governing amplitude variations and $\beta(r_\perp, z)$ controlling phase evolution. The amplitude reduction captured by $\alpha(r_\perp, z)$ encompasses both absorption (where photon energy is converted to other forms such as heat) and scattering (where photons are redirected from their original path), collectively contributing to wave attenuation. These are directly related to the physical properties through

$$\frac{\partial \alpha}{\partial z} = kn_0(1 + \Delta n)\kappa, \tag{2}$$

$$\frac{\partial \beta}{\partial z} = kn_0\left[\Delta n - \frac{\kappa^2}{2}\right], \tag{3}$$

where κ is the attenuation index. Physically, Eq. (2) describes how local absorption and scattering reduce wave amplitude—the factor $(1 + \Delta n)$ accounts for how refractive index variations modulate the effective absorption cross section. Equation (3) reveals that phase accumulation arises from two sources: direct contribution from refractive index variations (Δn term) and an indirect effect from absorption ($\kappa^2/2$ term). This quadratic absorption term, often overlooked, represents an additional phase shift that emerges from the complex nature of the optical potential when both refraction and absorption are present.

This decomposition strategy—separating the total refractive index field into mean-field and fluctuation field components—ensures mathematical convergence and physical interpretability. When $|\Delta n| < 1$, the fluctuation field remains bounded, preventing divergences that plague direct approaches. Moreover, this formulation naturally identifies the mean field n_0 with the spatial average over the field of view, which in biological imaging contains spatially distinct domains—intracellular regions ($n \approx 1.38$) and culture medium ($n \approx 1.33$). Since these domains are spatially separated, n_0 is well defined and Δn directly corresponds to measurable structural features like cell boundaries, organelles, or material interfaces. Minor refractive index fluctuations within the culture medium due to thermal or concentration gradients are negligibly small compared to these intracellular structural variations. Typical biological samples yield $|\Delta n| \sim 0.01$–0.1, well within the convergence condition $|\Delta n| < 1$. We emphasize that this formulation does not involve truncation of a Taylor series. The transport equations derived below are exact consequences of the paraxial wave equation for the decomposed field; the condition $|\Delta n| < 1$ enters as a physical requirement that fluctuations remain smaller than the mean field, not as a criterion for series convergence.

Expressing the complex amplitude in terms of observable quantities, $A = \sqrt{I}\, e^{i\varphi}$, and separating real and imaginary parts yields two coupled transport equations. From the imagi-

nary part emerges the generalized TIE:

$$\frac{\partial I}{\partial z} = -\frac{1}{kn_0}\nabla_\perp \cdot (I\nabla_\perp \varphi) - 2\frac{\partial \alpha}{\partial z} I. \tag{4}$$

We previously derived this generalized form of TIE in Ref. [11], where the first term represents Teague's original TIE describing intensity redistribution from phase gradients and the second term $-2(\partial\alpha/\partial z)$ captures direct intensity attenuation from absorption and scattering. This coupling reveals that intensity changes in heterogeneous media arise from both wave-front curvature and absorptive losses. In the pure-phase limit where $\kappa \to 0$, the attenuation term vanishes and Eq. (4) reduces to Teague's original TIE, recovering the conventional formulation as a special case.

From the real part emerges the transport of phase equation (TPE):

$$\frac{\partial \varphi}{\partial z} = \frac{\partial \beta}{\partial z} - \frac{1}{2kn_0}(\nabla_\perp \varphi)^2 + \frac{1}{2kn_0}\frac{\nabla_\perp^2 \sqrt{I}}{\sqrt{I}}. \tag{5}$$

Each term carries distinct physical meaning: $\partial\beta/\partial z$ represents the direct phase accumulation rate from optical path-length variations through heterogeneous media. The nonlinear term $-(\nabla_\perp\varphi)^2$ describes wave-front self-correction—regions with steep phase gradients experience additional phase retardation, analogous to self-focusing in nonlinear optics but arising here purely from propagation geometry. The final term $\nabla_\perp^2\sqrt{I}$ represents amplitude-phase coupling: intensity variations induce phase modulations through diffractive spreading, ensuring energy conservation during propagation. The derivation of the TPE is fully discussed in Appendix A.

Together, Eqs. (4) and (5) form a nondivergent system that rigorously describes wave propagation through complex media without assuming pure phase or weak absorption. The two equations are coupled through their shared dependence on both intensity and phase, and through the optical potential functions α and β that encode the medium's physical properties. It is this coupling that enables independent recovery of both Δn and κ from a single set of through-focus measurements.

III. RECONSTRUCTION ALGORITHM

The practical implementation of our framework requires extracting optical parameters from measurable intensity distributions. Consider through-focus intensity measurements at three planes: in-focus (I_0 at z_0) and symmetric defocus positions ($I_\pm$ at $z_0 \pm \Delta z$). For small propagation distances where the fluctuation field induces only linear changes in intensity (see Fig. 1), the intensity evolution follows:

$$I_\pm \approx I_0 \mp \frac{\Delta z}{kn_0}\nabla_\perp \cdot [I_0 \nabla_\perp \varphi_0] - 2I_0 \left.\frac{\partial \alpha}{\partial z}\right|_{z_0} \Delta z. \tag{6}$$

This equation reveals how defocused intensities encode both phase and absorption information. The antisymmetric component $(I_+ - I_-)$ isolates phase contributions, enabling retrieval through standard TIE solvers like the geometric multigrid method (GMGM) [12–15]. This yields phase distributions at z_0 and half-defocus positions $z_0 \pm \Delta z/2$ (see Fig. 1).

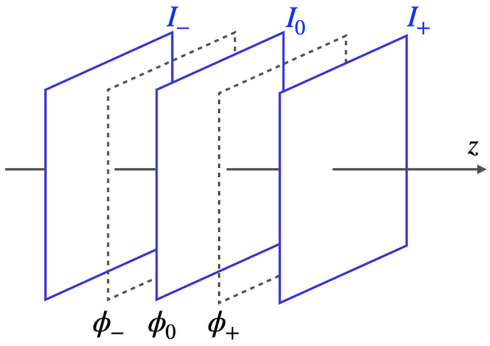


FIG. 1. Phase retrieval via TIE imaging typically involves a through-focus series of image intensities at three different z positions, $I(z_0 - \Delta z)$, $I(z_0)$, and $I(z_0 + \Delta z)$. These images are then used to compute the axial intensity derivatives, which, when combined with the intensity distributions at the in-focus and half of the defocus z positions, solves the TIE and reconstructs the phase distributions $\phi(z_0 - \Delta z/2)$, $\phi(z_0)$, and $\phi(z_0 + \Delta z/2)$.

The symmetric component $(I_+ + I_- - 2I_0)$ directly provides the intensity reduction parameter:

$$\left.\frac{\partial \alpha}{\partial z}\right|_{z_0} \approx \frac{I_+ + I_- - 2I_0}{-4\Delta z I_0}. \tag{7}$$

Physically, this symmetric difference isolates pure attenuation effects by canceling phase-induced intensity redistributions. Since phase gradients cause equal but opposite intensity changes at symmetric defocus positions, their contribution vanishes in the sum, leaving only the monotonic intensity decay from absorption.

With phase distributions at multiple planes, we compute axial phase derivatives $(\varphi_+ - \varphi_-)/\Delta z$ and apply the TPE to extract the phase-coupling parameter $\partial\beta/\partial z$. This quantifies how local refractive index variations and attenuation jointly influence phase evolution.

Finally, these intermediate parameters convert to physically meaningful quantities through

$$\Delta n \approx \frac{\partial_z \beta/kn_0 + (\partial_z \alpha/kn_0)^2/2}{1 - 2(\partial_z \beta/kn_0)}, \tag{8}$$

$$\mu = kn_0\kappa = \frac{\partial_z \alpha}{1 + \Delta n}, \tag{9}$$

where we assume $|\Delta n|^2 < 1$ for media with weak fluctuation fields. The refractive index fluctuation Δn directly relates to sample structure and composition, while the attenuation coefficient μ (units: 1/length) quantifies the total optical losses arising from both absorption and scattering processes in the medium. This reconstruction requires only three intensity measurements, which is much more efficient compared to tomographic approaches. The complete four-step reconstruction procedure, including the detailed implementation of the GMGM solver and intermediate parameter calculations, is provided in Appendix B.

IV. RECONSTRUCTION VALIDITY BOUNDS

A critical advancement of our framework is establishing explicit boundaries where reconstruction remains physically meaningful. These constraints emerge from fundamental

limits in both wave propagation physics and measurement capabilities.

The statistical reliability of reconstruction depends on the transmission probability through complex media:

$$P(\Delta z) = \int \Phi(k) e^{-2kn_0(1+\Delta n)\kappa\Delta z} dk, \tag{10}$$

where $\Phi(k)$ is the normalized spectral distribution of the incident beam with wave number k. The exponential term describes attenuation during propagation through absorbing media, with the attenuation factor depending on both the optical properties (Δn, κ) and propagation distance (Δz). From this probability distribution, we establish confidence intervals (e.g., 95%) that define the range within which true optical parameters lie, particularly critical near detection limits where intensity reductions or refractive-index variations challenge measurement reliability.

From photon counting statistics and diffraction physics emerge the fundamental validity bounds:

$$\left(\frac{2\Delta x}{\pi \Delta z}\right)^2 < \left|\Delta n - \frac{\kappa^2}{2}\right| < 1 - \frac{\kappa^2}{2}. \tag{11}$$

The lower bound has profound physical meaning: it represents the threshold where phase-induced intensity modulation becomes comparable to shot noise. The factor $(2\Delta x/\pi\Delta z)^2$ quantifies the minimum detectable phase gradient—determined by the ratio of pixel size to propagation distance (see Appendix C for the derivation). This transparent-limit regime is exemplified by unstained cells where $\mu \to 0$: phase contrast dominates but attenuation signals barely exceed photon shot noise. When phase variations occur over distances smaller than this diffraction length, their intensity signatures blur beyond recognition. This is not a limitation of detector technology but a fundamental consequence of wave physics: information encoded at spatial frequencies beyond the diffraction limit is irretrievably lost during propagation.

The upper bound ensures the paraxial approximation remains valid. As the fluctuation field $|\Delta n|$ approaches or exceeds unity—as seen in thick tissues or highly heterogeneous samples—ray angles become too large and higher-order diffraction becomes significant, thus breaking our framework. In this strong attenuation regime where $|\Delta n|$ approaches 0.5–1 or beyond, multiple scattering dominates. This is not merely reduced accuracy but fundamental failure of the underlying physics—the mean-field decomposition loses meaning when fluctuations become comparable to or larger than the mean field itself.

Understanding these regimes guides experimental design: choosing appropriate defocus distances, optimizing illumination conditions, and predicting reconstruction feasibility for a given experimental configuration.

V. EXPERIMENTAL VALIDATION

We validated our framework using two complementary systems: microlens arrays (MLA) as calibrated optical standards [16] and living HeLa cells as complex biological specimens. Experiments employed laser-scanning confocal microscopy and wide-field microscopy with various numerical apertures (NA = 0.45 for MLA, NA = 1.2 for HeLa cells, and NA = 1.49 for cell membranes). Complete optical configurations and results are in Appendix D.

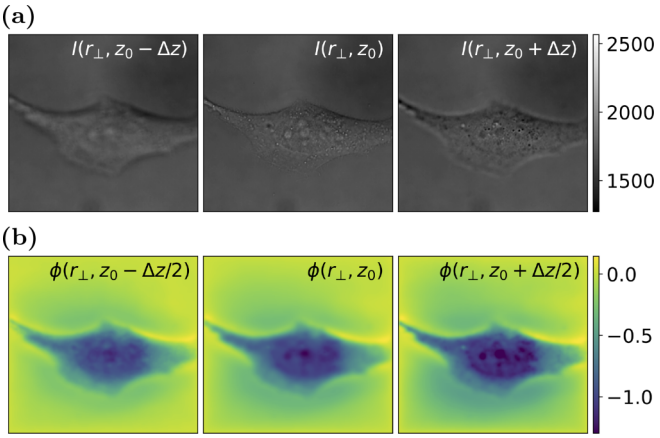


FIG. 2. Computational inputs of HeLa cells: (a) the image intensities (I_-, I_0, and I_+) and (b) the phases (ϕ_-, ϕ_0, and ϕ_+) reconstructed by using the GMGM.

For HeLa cells, we deliberately operated in the transparent-limit regime where attenuation signals approach statistical detection thresholds. This regime, characterized by $\mu \to 0$, provides a stringent test of the framework's ability to distinguish weak absorption signals from noise while maintaining stable reconstruction. Through-focus intensity stacks were acquired at $z_0 \pm 5$ μm with 488 nm illumination (see Fig. 2). The computational pipeline revealed rich optical heterogeneity despite weak signals. The intensity reduction parameter $\partial\alpha/\partial z$, extracted from the symmetric intensity component, mapped regions of absorption despite signals approaching noise levels. The phase-coupling parameter $\partial\beta/\partial z$, computed via TPE with axial phase derivatives, revealed how refractive index variations modulate local wave-front curvature.

Converting to physical parameters yielded spatial maps of refractive-index fluctuation field Δn [Fig. 3(a)] and attenuation coefficient field μ [Fig. 3(b)]. The Δn distribution clearly delineates cellular boundaries, nuclei, and organelles through refractive index contrast arising from the fluctuation field. The μ field, though noisier due to weak attenuation in the transparent-limit regime, still reveals cellular structure, with the sign indicating forward (positive) or backward (negative) wave propagation along the z axis.

Most revealing is the Δn-μ correlation plot shown in Fig. 3(c). The data cluster forms a characteristic pattern bounded by two distinct regions: (i) the green area representing the physical validity bounds from Eq. (11) and (ii) the black solid line indicating the 3σ statistical confidence level.

Analysis of multiple cells revealed that 0.2–25% of pixels fall outside the physical validity bounds, predominantly clustering near $\Delta n \approx 0$. At this point, the lower bound condition $(2\Delta x/\pi\Delta z)^2$ becomes the limiting factor—these pixels represent regions where refractive index variations fall below the detection threshold and should be interpreted as $\Delta n \approx 0$. Importantly, these outliers remain within the 3σ statistical confidence interval, confirming that the framework correctly identifies the transition between measurable and subthreshold regions while maintaining mathematical stability.

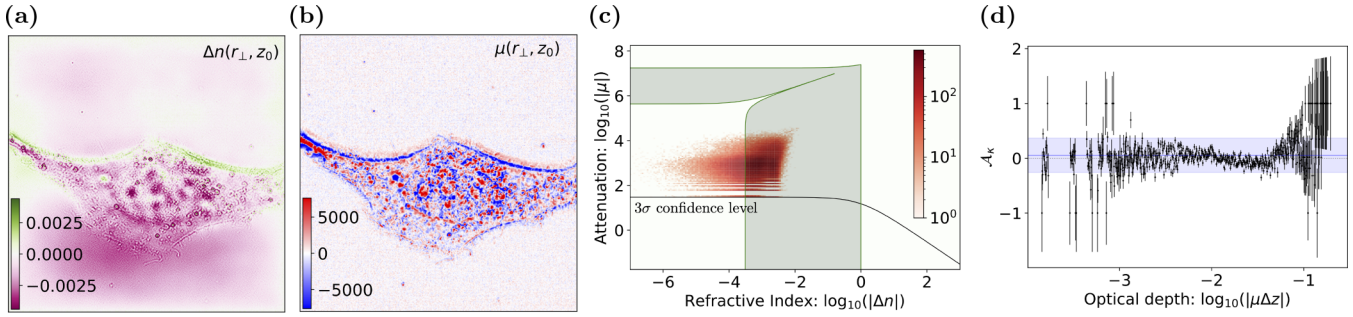


FIG. 3. Results for HeLa cells. (a) Spatial distribution of refractive-index fluctuations $\Delta n(r_\perp, z_0)$ and (b) attenuation coefficients $\mu(r_\perp, z_0)$. The sign of the $\mu(r_\perp, z_0)$ indicates forward and backward wave propagations along the z axis. (c) Correlation patterns between $\Delta n(r_\perp, z_0)$ and $\mu(r_\perp, z_0)$. The black solid line is the 3σ confidence level. 65 055 events (24.82%) fall outside the physical parameter boundaries (i.e., green area) given by Eq. (11), where reconstruction remains physically consistent despite operating in the transparent-limit regime. (d) Measured value of the asymmetry $\mathcal{A}_\kappa$ in bins of the optical depth $\log_{10}|\mu\Delta z|$. The blue line and bands are the statistical average and the root-mean-squared (RMS) value, respectively. Dashed line represents $\mathcal{A}_\kappa = 0$.

To verify the generality of our framework across different sample types and imaging modalities, we extended our validation to additional systems. MLA measurements (see Fig. 4 in Appendix D 1) provided complementary validation with well-defined optical elements, showing only 3.2% of pixels outside validity bounds but well within the 3σ confidence level. Wide-field microscopy with xenon lamp illumination of HeLa cell membranes (see Fig. 5 in Appendix D 1) tested versatility across illumination modalities, with membrane-specific optical signatures emerging clearly in both fields and minimal outliers (0.2%).

In addition to statistical uncertainties, finite numerical aperture (NA) introduces systematic errors because high-NA objectives collect rays at angles where the paraxial approximation breaks down. We parametrize this deviation through $\epsilon = \mathrm{NA}^2/4m^2$ and propagate it through the reconstruction chain: systematic biases in Δn scale quadratically with NA/m, while μ remains minimally affected in the transparent limit (see Appendix D 2 for the full derivation and quantitative error estimates).

VI. SYMMETRY IN WAVE PROPAGATION

An important implication of the coupled TIE-TPE framework is the emergence of attenuation symmetry in wave propagation, a property that has not been quantitatively examined in this context. The attenuation index κ can take positive or negative values, corresponding to forward (transmission) and backward (reflection) propagation modes. When the medium exhibits optical reciprocity, the propagation probability $\mathcal{P}(\kappa) = \exp[-2kn_0(1+\Delta n)\kappa\Delta z]$ should remain unchanged under directional inversion $\kappa \to -\kappa$, which we quantify through the asymmetry parameter:

$$\mathcal{A}_\kappa = \frac{\mathcal{P}(+\kappa) - \mathcal{P}(-\kappa)}{\mathcal{P}(+\kappa) + \mathcal{P}(-\kappa)}, \tag{12}$$

where $\mathcal{P}(+\kappa)$ and $\mathcal{P}(-\kappa)$ represent propagation probabilities for forward and backward modes, respectively. Perfect symmetry yields $\mathcal{A}_\kappa = 0$, while nonzero values would indicate deviations from reciprocity arising from effects such as magneto-optical interactions or structural chirality.

Our experimental measurements of $\mathcal{A}_\kappa$ versus optical depth $\log_{10}|\mu\Delta z|$ for HeLa cells [Fig. 3(d)] show that $\mathcal{A}_\kappa$ remains statistically consistent with zero across three orders of magnitude. The measured values fluctuate within the statistical uncertainty (RMS bands) around zero, with no systematic deviation observed across the entire optical depth range.

This invariance is consistent with the preservation of optical reciprocity under the experimental conditions studied. In the weak scattering regime (optical depth $<10^{-2}$), where our paraxial approximation is most valid, the symmetry confirms that microscopic scattering events preserve time-reversal invariance. Even as optical depth increases toward unity—approaching the limits of our framework—the symmetry persists, suggesting robustness beyond the strict validity regime of Eq. (11).

The observed $\mathcal{A}_\kappa$ invariance indicates that biological tissues maintain optical reciprocity at the wavelength scale, preserving identical light-matter interactions in forward and backward propagation. This reciprocity provides a consistency condition for quantitative phase measurements under bidirectional propagation. This quantitative experimental examination of attenuation symmetry in biological samples supports the consistency of our theoretical framework with reciprocity-based imaging principles. Measurements on microlens arrays and HeLa cell membranes show similar invariance, with detailed analysis in Appendix D 1.

VII. CONCLUSION

We have presented a coupled TIE-TPE framework for quantitative retrieval of refractive-index fluctuations and attenuation coefficients in heterogeneous optical media. The framework is derived from the paraxial wave equation with a complex optical potential, using Reynolds decomposition to separate the refractive index field into a spatially uniform mean field and a local fluctuation field. This formulation yields a nondivergent system of transport equations that handles both refraction and attenuation without requiring linearization or weak-absorption approximations.

A central result of this work is the derivation of explicit validity bounds that define the measurable parameter space for a given experimental configuration. The lower bound, set by photon counting statistics and the diffraction limit, determines the minimum detectable signal; the upper bound, set by the

paraxial condition $|\Delta n| < 1$, determines where the framework ceases to be applicable. Together, these bounds provide experimentally verifiable criteria for assessing reconstruction feasibility before measurements are performed, distinguishing our approach from methods where validity domains remain implicit.

Experimental validation using microlens arrays, HeLa cells, and HeLa cell membranes demonstrated robust reconstruction across distinct optical regimes, including the transparent-limit regime where attenuation signals approach detection thresholds. The correlation between reconstructed Δn and μ values fell within the theoretically predicted validity regions across all samples tested, with only 0.2–25% of pixels outside the physical parameter boundaries.

The measurements further revealed that the attenuation asymmetry parameter $\mathcal{A}_\kappa$ remains consistent with zero across three orders of magnitude in optical depth, indicating preservation of optical reciprocity in structurally heterogeneous biological media. This invariance was observed across all three sample types and proved robust against systematic errors from finite numerical aperture effects, with systematic-to-statistical error ratios remaining below 0.07 even at NA = 1.49 (see Appendix D 2).

Several limitations of the current framework should be noted. The paraxial approximation restricts applicability to media where ray angles remain small relative to the optical axis; thick tissues or strongly heterogeneous samples where fluctuations become comparable to the mean field fall outside the valid regime. The framework is formulated for monochromatic illumination and does not account for chromatic dispersion or wavelength-dependent scattering. Extension to partially coherent illumination, which is relevant for many biological imaging configurations, would require modification of the transport equations.

Looking ahead, the explicit validity bounds established here may serve as design criteria for optimizing experimental configurations in quantitative phase imaging. The observed preservation of attenuation symmetry in biological media, if confirmed across a broader range of sample types and imaging conditions, could provide a useful self-consistency check for phase retrieval algorithms operating in heterogeneous media. Extension of the framework to three-dimensional tomographic reconstruction—combining the coupled TIE-TPE equations with angular diversity—represents a natural direction for future work.

ACKNOWLEDGMENTS

The authors express their sincere gratitude to M. Hattori, N. Yoneda, and O. Matoba for their invaluable guidance and support throughout this research. We also acknowledge E. Watanabe for helpful discussions on the effective use of AI tools such as Claude (claude.ai, Anthropic) and ChatGPT (chatgpt.ai, OpenAI) for computational and manuscript preparation assistance. This work was supported by the Japan Society for the Promotion of Science (JSPS) KAKENHI Grants No. JP20H05891, No. JP20K21836, No. JP21H05605, No. JP22H04926, No. JP23K17364, and No. JP23K26795. Additional support was provided by the Asahi Glass Foundation, the Frontier Photonic Sciences Project of National Institutes of Natural Sciences (NINS) Grant No. 01212504, and by the Joint Research of the Exploratory Research Center on Life and Living Systems (ExCELLS) through the ExCELLS Encouragement Research Program for Young Scientists.

J.S. and H.Y. performed the experiments.

DATA AVAILABILITY

The data that support the findings of this article are openly available [17], embargo periods may apply.

APPENDIX A: DERIVATION OF THE TPE

Separating the paraxial wave equation [i.e., Eq. (1) in the main text] into the real and imaginary sections, the TIE can be derived in the imaginary part (see Sec. A 1 of the Supplemental Material in Ref. [11] for derivation). Conversely, the TPE can be derived in the real part and its derivation is given as follows.

In the real part of the paraxial wave equation,

$$
\begin{aligned}
\mathrm{Re}\left[\nabla_\perp^2 A + 2kn_0 i\frac{\partial A}{\partial z} + 2kn_0\frac{\partial}{\partial z}(\beta + i\alpha)A\right] &= 0,\\
\mathrm{Re}\left[\nabla_\perp^2\sqrt{I}e^{i\phi} + 2kn_0 i\frac{\partial}{\partial z}\sqrt{I}e^{i\phi} + 2kn_0\frac{\partial}{\partial z}(\beta + i\alpha)\sqrt{I}e^{i\phi}\right] &= 0,\\
\mathrm{Re}\left[\nabla_\perp^2\sqrt{I}e^{i\phi} + 2kn_0 i\left(\frac{\partial\sqrt{I}}{\partial z}e^{i\phi} + \sqrt{I}\frac{\partial e^{i\phi}}{\partial z}\right)\right] + 2kn_0\frac{\partial\beta}{\partial z}\sqrt{I}e^{i\phi} &= 0,\\
\mathrm{Re}\left[\nabla_\perp^2\sqrt{I}e^{i\phi} + 2kn_0 i\sqrt{I}\frac{\partial e^{i\phi}}{\partial z}\right] + 2kn_0\frac{\partial\beta}{\partial z}\sqrt{I}e^{i\phi} &= 0,\\
\mathrm{Re}[\nabla_\perp^2\sqrt{I}e^{i\phi}] - 2kn_0\sqrt{I}\frac{\partial\phi}{\partial z}e^{i\phi} + 2kn_0\frac{\partial\beta}{\partial z}\sqrt{I}e^{i\phi} &= 0,\\
\mathrm{Re}[(\nabla_\perp^2\sqrt{I})e^{i\phi} + 2(\boldsymbol{\nabla}_\perp\sqrt{I})(\boldsymbol{\nabla}_\perp e^{i\phi}) + \sqrt{I}(\nabla_\perp^2 e^{i\phi})] - 2kn_0\sqrt{I}\frac{\partial\phi}{\partial z}e^{i\phi} + 2kn_0\frac{\partial\beta}{\partial z}\sqrt{I}e^{i\phi} &= 0,\\
[\nabla_\perp^2\sqrt{I} - \sqrt{I}(\boldsymbol{\nabla}_\perp\phi)^2] - 2kn_0\sqrt{I}\frac{\partial\phi}{\partial z} + 2kn_0\sqrt{I}\frac{\partial\beta}{\partial z} &= 0. \qquad \text{(A1)}
\end{aligned}
$$

Divided by $2kn_0\sqrt{I}$, we can deduce the TPE,

$$\frac{\partial\phi}{\partial z} = \frac{\partial\beta}{\partial z} - \frac{1}{2kn_0}(\nabla_\perp\phi)^2 + \frac{1}{2kn_0}\frac{\nabla_\perp^2\sqrt{I}}{\sqrt{I}}, \tag{A2}$$

where the axial derivative of $\alpha(r_\perp, z)$ vanishes through this modification.

The last term in the Eq. (A2) can be rewritten as follows:

$$\frac{\nabla_\perp^2\sqrt{I}}{\sqrt{I}} = \frac{1}{\sqrt{I}}\nabla_\perp\cdot\left(\frac{\nabla_\perp I}{2\sqrt{I}}\right) = \frac{\sqrt{I}\left(\nabla_\perp^2 I\right) - (\nabla_\perp\sqrt{I})(\nabla_\perp I)}{2I\sqrt{I}} = \frac{2I\left(\nabla_\perp^2 I\right) - (\nabla_\perp I)^2}{4I^2}.$$

Inserting this back to Eq. (A2), the TPE can also be written in the form of

$$\frac{\partial\phi}{\partial z} = \frac{\partial\beta}{\partial z} - \frac{1}{2kn_0}(\nabla_\perp\phi)^2 + \frac{1}{4kn_0}\left(\frac{\nabla_\perp^2 I}{I}\right) - \frac{1}{8kn_0}\left(\frac{\nabla_\perp I}{I}\right)^2. \tag{A3}$$

APPENDIX B: RECONSTRUCTION METHOD

Our reconstruction algorithm, developed to systematically recover optical turbulence and interactions in heterogeneous media, consists of four sequential steps.

(1) As the first step of our linear perturbation approach along the longitudinal axis, we reconstruct the phase distribution ϕ_0 at the in-focus position by utilizing the axial asymmetric component of the Eq. (3) in the main text:

$$\frac{I_+ - I_-}{2\Delta z} \approx -\frac{1}{kn_0}\nabla_\perp\cdot[I_0\nabla_\perp\phi_0], \tag{B1}$$

where I_0 and $I_\pm$ are the inputs of image intensities at the in-focus (z_0) and defocus positions ($z_0 \pm \Delta z$). This differential equation represents a Poisson equation that we solve using a geometric multigrid method (GMGM) [12–14,18]. The multigrid approach provides efficient numerical solutions by operating on multiple resolution levels simultaneously, which significantly accelerates convergence compared to single-grid iterative methods. Our implementation employs a V-cycle scheme with Gauss-Seidel relaxation, which effectively handles both low and high spatial frequency components of the phase distribution while maintaining computational efficiency for large data sets. This approach is particularly advantageous for handling the boundary conditions and nonuniformities in intensity that are common in experimental data.

Also, we apply the same GMGM technique to retrieve phase distributions at the half-defocus positions $\phi_\pm$ using

$$\frac{I_\pm - I_0}{\Delta z} \approx -\frac{1}{kn_0}\nabla_\perp\cdot[I_{\pm1/2}\nabla_\perp\phi_\pm], \tag{B2}$$

where the intensity at half-defocus positions is estimated as $I_{\pm1/2} = (I_0 + I_\pm)/2$.

(2) The intensity reduction parameter $\partial\alpha/\partial z$ is extracted by leveraging the axial symmetric component of Eq. (6) in the main text:

$$I_+ \approx I_0 - \frac{\Delta z}{kn_0}\nabla_\perp\cdot[I_0\nabla_\perp\varphi_0] - 2I_0\left.\frac{\partial\alpha}{\partial z}\right|_{z_0}\Delta z,$$

$$I_- \approx I_0 + \frac{\Delta z}{kn_0}\nabla_\perp\cdot[I_0\nabla_\perp\varphi_0] - 2I_0\left.\frac{\partial\alpha}{\partial z}\right|_{z_0}\Delta z.$$

Adding those equations, we obtain

$$I_+ + I_- \approx 2I_0 - 4I_0\left.\frac{\partial\alpha}{\partial z}\right|_{z_0}\Delta z.$$

Finally, the reduction parameter can be deduced as follows:

$$\left.\frac{\partial\alpha}{\partial z}\right|_{z_0} \approx \frac{I_+ + I_- - 2I_0}{-4I_0\Delta z}. \tag{B3}$$

This parameter captures how the wave field's intensity attenuates during propagation due to absorptive and scattering properties of the medium.

(3) The phase-coupling parameter $\partial\beta/\partial z$ is computed by utilizing the TPE together with axial phase derivatives $\partial\phi/\partial z \approx (\phi^+ - \phi^-)/\Delta z$:

$$\left.\frac{\partial\beta}{\partial z}\right|_{z_0} \approx \frac{\phi_+ - \phi_-}{\Delta z} + \frac{1}{2kn_0}\left[\nabla_\perp\phi_0\right]^2 - \frac{1}{2kn_0}\frac{\nabla_\perp^2\sqrt{I_0}}{\sqrt{I_0}}. \tag{B4}$$

This intermediary parameter effectively quantifies how local phase variations influence wave-front deformation during propagation.

(4) Finally, the intermediary parameters $\partial\alpha/\partial z$ and $\partial\beta/\partial z$ are converted into physically meaningful quantities: the spatial distributions of refractive-index fluctuation and attenuation coefficients. The conversion functions are given by Eqs. (8) and (9) in the main text.

These transformations establish a direct link between measurable wave field properties (intensity and phase) and the fundamental optical properties of the medium (refractive index and attenuation), enabling comprehensive characterization of heterogeneous optical media from a minimal set of through-focus measurements.

APPENDIX C: RECONSTRUCTION LIMITS

The physical lower bound of the reconstruction method is fundamentally governed by the signal-to-noise ratio (SNR) of the detector's photon counting capability, which must exceed unity for meaningful reconstruction. This constraint emerges through a systematic two-stage derivation process.

First, we establish the lower bound for TIE-based phase retrieval. The fundamental constraint emerges from the requirement that intensity differences ΔI between the defocus

image distances $2\Delta z$ must exceed the shot-noise limit,

$$\Delta I = \left| -\frac{1}{kn_0} \int_{z_0-\Delta z}^{z_0+\Delta z} \nabla_\perp \cdot [I \nabla_\perp \phi] dz \right| > \sqrt{I(z_0) + I_{bg}}, \tag{C1}$$

where Δz and kn_0 are the defocus lateral distance and the wave number of signaling photons in the mean refractive index field, respectively. I_{bg} is intensity distributions in background.

For the sake of simplicity, we assume constant image intensity (i.e., $I_0 = \text{const}$) and sinusoidal phase distributions [i.e., $\phi = \phi_0 \sin(k_x x) k_z (z - z_0)$]. This constraint translates directly into a minimum detectable phase amplitude. In this assumption, we modify Eq. (C1) to find that the minimum detectable phase variation,

$$|\phi| > \phi_{\min} = \frac{kn_0 \sqrt{I_0 + I_{bg}}}{\Delta z \, k_x^2 \, I_0} = \frac{kn_0 \Delta z}{SNR} \left(\frac{2\Delta x}{\pi \Delta z} \right)^2, \tag{C2}$$

where we assume the minimum spatial frequency $k_x = 2\pi/4\Delta x$ for phase signal detection. Further details are discussed in Ref. [18].

Building upon this foundation, we then derive the lower limit for the β-derivative intermediary function. Substituting our sinusoidal phase assumption and constant intensity to the TPE [i.e., Eq. (5) in the main text], we obtain

$$\begin{aligned}
\frac{\partial \beta}{\partial z} &= \frac{\partial \phi}{\partial z} + \frac{1}{2kn_0} (\nabla_\perp \phi)^2 - \frac{1}{2kn_0} \frac{\nabla_\perp^2 \sqrt{I}}{\sqrt{I}} \\
&= \phi_0 \sin(k_x x) k_z + \frac{1}{2kn_0} \left(k_x \phi_0 \cos(k_x x) k_z \Delta z \right)^2 \\
&\quad - \frac{1}{2kn_0} \frac{\nabla_\perp^2 \sqrt{I_0}}{\sqrt{I_0}} \\
&= \frac{\phi_0 \sin(k_x x) k_z \Delta z}{\Delta z} + \frac{1}{2kn_0} (k_x \phi_0 k_z \Delta z)^2 \left(1 - \sin^2(k_x x) \right) \\
&= \frac{\phi}{\Delta z} + \frac{1}{2kn_0} \left(k_x \phi_0 \sin(k_x x) k_z \Delta z \right)^2 \left(\frac{1}{\sin^2(k_x x)} - 1 \right) \\
&= \frac{\phi}{\Delta z} + \frac{1}{2kn_0} (k_x \phi)^2 \left(\frac{1}{\sin^2(k_x x)} - 1 \right).
\end{aligned} \tag{C3}$$

Inserting Eq. (C2) into Eq. (C3), the β-derivative intermediary parameter can be limited as follows:

$$\left| \frac{\partial \beta}{\partial z} \right| > \frac{\phi^{\min}}{\Delta z} + \frac{1}{2kn_0} \left(k_x \phi^{\min} \right)^2 \cancelto{0}{\left(\frac{1}{\sin^2(k_x x)} - 1 \right)}, \tag{C4}$$

where the nonlinear term vanishes as $\sin^2(k_x x) \to 1$. Dividing by kn_0 and setting $SNR = 1$ at observable minimum, we systematically arrive at the final constraint:

$$\left| \Delta n - \frac{1}{2} \kappa^2 \right| > \left(\frac{2\Delta x}{\pi \Delta z} \right)^2. \tag{C5}$$

This derived physical lower bound characterizes the fundamental limit where spatial frequencies approach the critical diffraction threshold, causing irreversible information loss in the measurements. As the $\Delta x/\Delta z$ ratio increases—either due to poorer spatial resolution or decreased propagation distance—the minimum detectable refractive index variation increases quadratically, thus significantly reducing the method's sensitivity to fine-structural features within the sample.

APPENDIX D: ANALYSIS

1. Microscopy configuration

Configuration details for bright-field imaging systems are described as follows.

(1) Laser-scanning confocal microscope [4]. Bright-field imaging was performed using a Nikon A1 Rsi confocal system equipped with a PlanApo 10× (NA = 0.45; Nikon, Tokyo, Japan) and a PlanApo-VC 60 × A water-immersion objective lens (NA = 1.2; Nikon) at room temperature. As illustrated in Fig. 4(a), the illumination laser beam is directed to a confocal scanner unit through a series of relay optics and is reflected by a dichroic mirror (DM). The beam is then scanned by a Galvano scanner (GS) and focused onto the physical and biological samples by the objective lens. The transmitted light is collected by a condenser lens of Köller illumination optics and is then relayed to a photodetector without a pinhole, allowing efficient signal collection for phase retrieval based on TIE.

(i) Physical sample. The MLA300-14AR-M, a precision-fabricated microlens array (MLA) from Thorlabs housed in a $\phi 1''$ mount (25.4 mm diameter and 3.5 mm thickness) compatible with standard optomechanical components [16], was employed for testing the reconstruction performance. This array consists of a 10×10 mm^2 fused silica substrate patterned with square plano-convex microlenses (295 μm side length and 300 μm pitch) arranged in a regular square grid. The lenslets were fabricated using photolithographic processes to ensure high positional accuracy and shape uniformity. A broadband antireflection (AR) coating optimized for the 400−900 nm wavelength range was applied, reducing surface reflectivity to below 1%. The array provides an effective focal length of 14.6 mm and a fill factor of approximately ∼96.7%, enabling efficient optical coupling. The MLA was observed using PlanApo 10× objective lens.

Parameters: wavelength of illumination light, $\lambda =$ 488 nm; defocus distance, $\Delta z = 100$ μm; the scanning pitch, 0.621 μm; magnification, ×10; image pixel length, $\Delta x = \Delta y = 1.24$ μm; total number of z-stack images, 41 image took 19 min; image size, 1024 × 1024 pixels; beam flux, $\Phi(k) = \delta(k - k_\lambda)$; see Fig. 4(f) for parameter allowed region in the $\Delta n(r_\perp, z_0)$-$\mu(r_\perp, z_0)$ spaces (i.e., green area).

Results are shown in Fig. 4. The MLA system serves as a calibrated reference with well-characterized optical properties, enabling direct comparison between reconstructed and nominal values. The periodic lens structure is clearly resolved in both Δn and μ fields, with the reconstructed Δn values consistent with the known refractive index contrast between fused silica and air. Only 3.2% of pixels fall outside the physical validity bounds, predominantly in interlens regions where the optical path difference approaches the detection threshold. These results validate the reconstruction pipeline under controlled conditions before application to biological specimens.

(ii) Biological sample. HeLa cells (RCB0007, RIKEN Cell Bank, Tsukuba, Japan) were cultured in culture

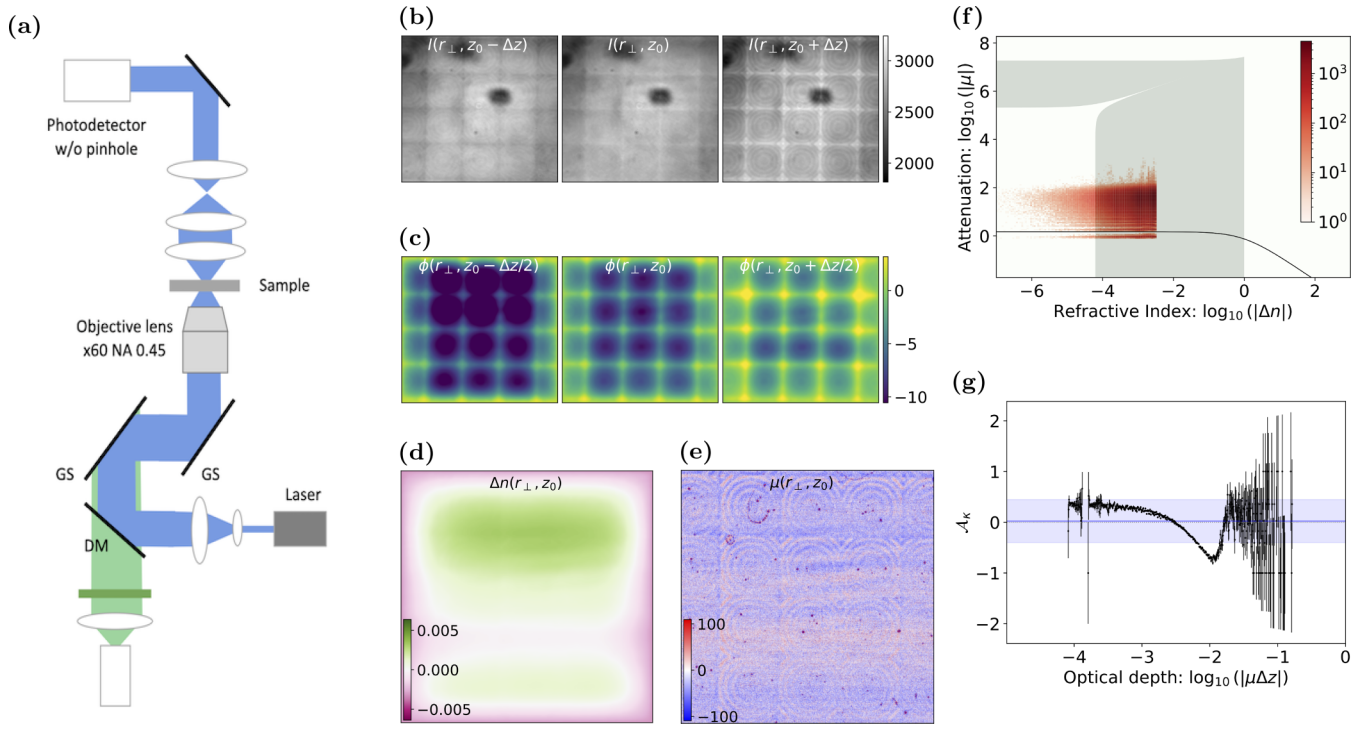


FIG. 4. Results for the MLA sample. (a) Optical path for the bright-field imaging systems with laser-scanning confocal microscope. (b) Intensity distributions, $I(r_\perp, z_0 - \Delta z)$, $I(r_\perp, z_0)$, and $I(r_\perp, z_0 + \Delta z)$. (c) Phase distributions reconstructed from the three fluorescent cell images. (d) Reconstructed distributions of the refractive-index fluctuations and (e) attenuation coefficients. (f) Correlation pattern between $\Delta n(r_\perp, z_0)$ and $\mu(r_\perp, z_0)$ lies with the 3σ confidence level (i.e., black solid line). 33 233 events (3.169%) fall outside the physical parameter boundaries (i.e., green area) given by Eq. (11) in the main text. (g) Asymmetry property as a function of optical depth. Blue line and bands in the asymmetry property plots are the statistical average and the root-mean-squared (RMS) value, respectively. Dashed line represents $\mathcal{A}_\kappa = 0$.

medium: Dulbecco's modified essential medium (11965-092, Thermo Fisher Scientific, Walthum, MA, USA) supplemented with 10% fetal bovine serum (FBS; 10437, Invitrogen) and penicillin/streptomycin (PS; 15140-122, ThermoFisher) at 37 °C under humidified 5% CO2 atmosphere until observation. Before observation, the culture medium to imaging medium; DMEM without phenol red (21063-029, ThermoFisher) supplemented with 10% FBS and PS.

Parameters: wavelength of illumination light, $\lambda = 488$ nm; defocus distance, $\Delta z = 5.00$ μm; image pixel length, $\Delta x = \Delta y = 0.138$ μm; total number of z-stack images, 81 frames image took 4.7 min; image size, 512×512 pixels; beam flux, $\Phi(k) = \delta(k - k_\lambda)$; see Fig. 3(c) for parameter allowed region in the $\Delta n(r_\perp, z_0)$-$\mu(r_\perp, z_0)$ spaces (i.e., green area).

Results are shown in Figs. 2 and 3 in the main text. The HeLa cell system operates in the transparent-limit regime where attenuation signals approach statistical detection thresholds, testing whether the framework maintains stable reconstruction when $\mu \to 0$. Cellular boundaries and organelles are clearly resolved in the Δn field, while the μ field reveals spatially correlated attenuation structure despite the weak signals. The $\mathcal{A}_\kappa$ measurement across three orders of magnitude in optical depth provides the central test of reciprocity invariance in biological media.

(2) Wide-field microscope. Bright-field observation experiments were conducted using home-built objective-type total internal reflection fluorescence microscopes (TIRFM) based on inverted microscopes (IX81; Olympus Corp.) [19]. As illustrated in Fig. 5(a), illumination was provided by a Xenon lamp (SLS401 Light Source with Xenon Arc Lamp for 240–2400 nm, 5800 K, Thorlabs) [20], with the beam first collimated and then filtered through a bandpass excitation filter (BF 525/30, Semrock Inc.) to select the desired wavelength range. The light was then reflected by a dichroic mirror (DM) and directed toward the biological sample (i.e., HeLa cells) through a high numerical aperture oil-immersion objective lens (100×, NA 1.49; Olympus Corp.). After interacting with the sample, the transmitted light was collected by the same objective and passed through an emission optical train that included a second dichroic mirror (DM R561, Semrock Inc.) and an emission bandpass filter (BF 525/50, Semrock Inc.). The filtered emission signal was finally focused onto an electron-multiplying CCD (EMCCD) camera (ImagEM; Hamamatsu Photonics Inc.) for image acquisition.

(i) Parameters: wavelength of emission light, $\lambda = 525$ nm; defocus distance, $\Delta z = 5$ μm; image pixel length, $\Delta x = \Delta y = 80$ nm; total number of z-stack images, 41 frames, and image size, 512×512 pixels; beam flux, $\Phi(k) = \Phi_{Xe}$ [20]; see Fig. 5(f) for parameter allowed region in the $\Delta n(r_\perp, z_0)$-$\mu(r_\perp, z_0)$ spaces (i.e., green area).

Results are shown in Fig. 5. This configuration tests the framework under the most demanding conditions: wide-field (nonlaser) illumination with the highest numerical aperture (NA = 1.49, oil immersion). Despite these

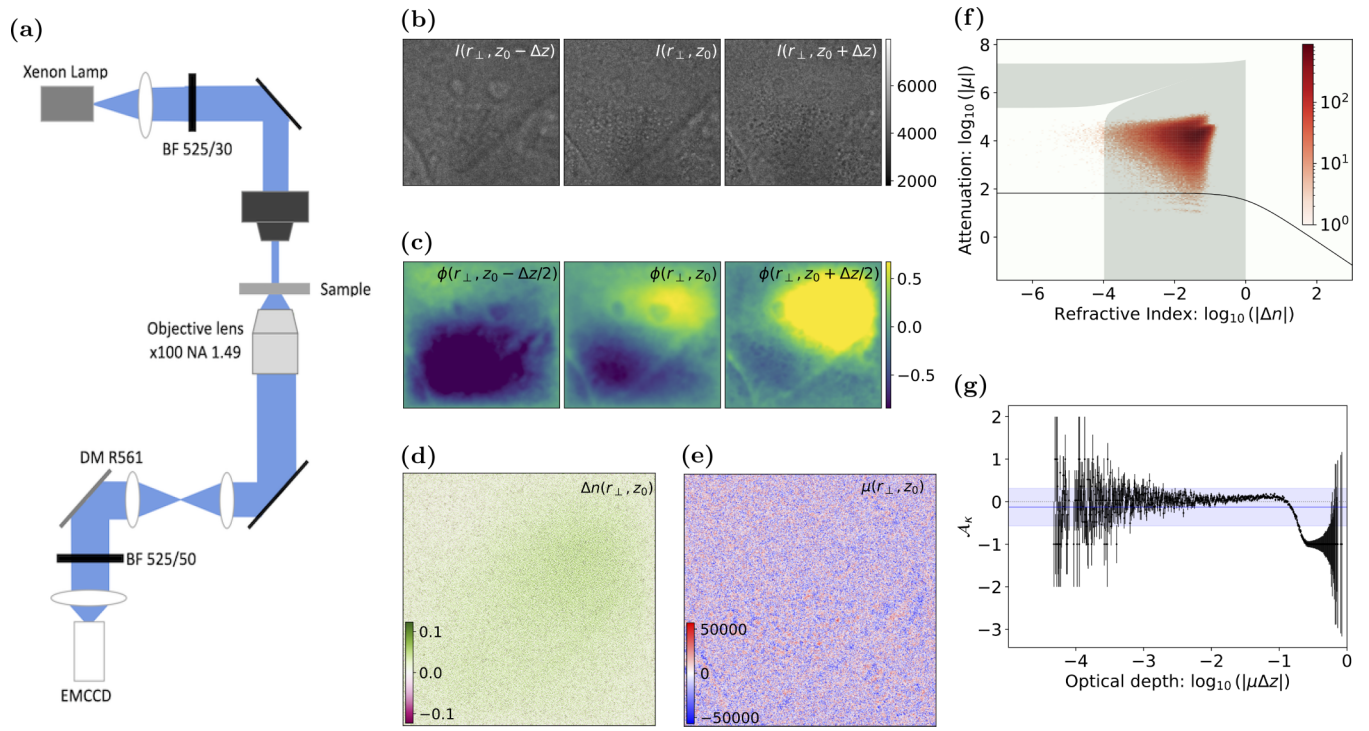


FIG. 5. Results for the HeLa cell membrane. (a) Optical path for the bright-field imaging systems with wide-field microscope. (b) Intensity distributions, $I(r_\perp, z_0 - \Delta z)$, $I(r_\perp, z_0)$, and $I(r_\perp, z_0 + \Delta z)$. (c) Phase distributions reconstructed from the three fluorescent cell images. (d) Reconstructed distributions of the refractive-index fluctuations and (e) attenuation coefficients. (f) Correlation pattern between $\Delta n(r_\perp, z_0)$ and $\mu(r_\perp, z_0)$ lies with the 3σ confidence level (i.e., black solid line). 555 events (0.217%) fall outside the physical parameter boundaries (i.e., green area) given by Eq. (11) in the main text. (g) Asymmetry property as a function of optical depth. Blue line and bands in the asymmetry property plots are the statistical average and the root-mean-squared (RMS) value, respectively. Dashed line represents $\mathcal{A}_\kappa = 0$.

challenges, membrane-specific optical signatures emerge clearly in both the Δn and μ fields, demonstrating that the coupled TIE-TPE framework is not restricted to laser-scanning modalities. The exceptionally low outlier fraction (0.2%) reflects the stronger optical contrast at membrane interfaces compared to intracellular structures. The $\mathcal{A}_\kappa$ measurement under this highest-NA configuration provides the most stringent test of reciprocity invariance against systematic errors from finite aperture effects.

2. Systematic uncertainties from finite numerical aperture

High numerical aperture (NA) objectives are essential for achieving high lateral resolution in microscopy, particularly when imaging subcellular structures. However, the use of high-NA optics introduces systematic deviations from the paraxial approximation that underlies the TIE theory. While the transverse (x-y) plane benefits from improved resolution through larger collection angles (following the Abbe limit $\lambda/2\mathrm{NA}$), the axial (z-direction) propagation experiences significant departures from paraxial wave theory.

The fundamental challenge arises because TIE formulation assumes paraxial wave propagation with small angles relative to the optical axis. High-NA objectives, however, collect rays at angles up to $\theta_{\max} = \sin^{-1}(\mathrm{NA}/m)$, which can exceed 60° for NA > 1.2 in aqueous media. m denotes the refractive index of the objective lens immersion medium. For instance, with NA = 1.20 in water ($m = 1.33$), the maximum collection angle reaches approximately 64.5°, where $\sin\theta \approx 0.90$ significantly deviates from the paraxial approximation $\sin\theta \approx \theta$.

a. Mathematical framework for NA-effect quantification

To quantify the systematic errors introduced by finite NA, we develop an effective model that accounts for the angular distribution of rays within the collection cone and derive how this modification propagates through the TIE reconstruction.

(1) *Effective model.* In high-NA systems, light rays propagate at various angles relative to the optical axis, up to a maximum angle $\theta_{\max} = \arcsin(\mathrm{NA}/m)$. For a ray at angle θ, the z component of the wave vector is $k_z = kn_0\cos\theta$, where $k = 2\pi/\lambda$ is the vacuum wave number and n_0 is the medium refractive index. To account for the contribution of all rays within the NA cone, we need to calculate the average z component of the wave vector.

TABLE I. *System parameters*. Experimental parameters for the three imaging systems. The dimensionless parameter ϵ quantifies the deviation from the paraxial approximation and determines the magnitude of systematic errors.

System	NA	m	Δz (μm)	$\epsilon = \mathrm{NA}^2/4m^2$
MLA	0.45	1.00	100	0.050625
HeLa cells	1.20	1.33	5	0.203607
Cell membrane	1.49	1.515	5	0.241683

TABLE II. *Error estimations of refractive index fluctuations (Δn).* Systematic errors in Δn increase quadratically with NA/m. The systematic error becomes comparable to statistical uncertainty for the oil-immersion objective (NA = 1.49), indicating that NA correction is essential for high-NA quantitative phase measurements.

System	Measured Δn	Statistical RMS	Relative error	Systematic shift	$\sigma_{\text{syst}}/\sigma_{\text{stat}}$
MLA	0.001333	±0.000942	+10.649%	0.000142	0.150721
HeLa	0.001018	±0.000931	+51.041%	0.000520	0.558309
Cell membrane	0.029664	±0.022071	+63.801%	0.018934	0.857855

Assuming uniform intensity distribution within the collection cone (a first-order approximation), the effective wave vector along z becomes $\langle k_z\rangle = kn_0\langle\cos\theta\rangle$. In the paraxial approximation, $\cos\theta \approx 1-\theta^2/2$ for small angles. Averaging over the NA cone, we obtain $\langle\cos\theta\rangle \approx 1-\langle\theta^2\rangle/2$. For uniform distribution up to $\theta_{\max}$, this gives $\langle\cos\theta\rangle \approx 1-\theta_{\max}^2/4$.

Using the relation $\sin\theta_{\max} = \text{NA}/m$, and for moderate NA values where $\theta_{\max} \approx \sin\theta_{\max}$, we find $\theta_{\max}^2 \approx \text{NA}^2/m^2$. This leads to the effective refractive index:

$$n_{\text{eff}} = n_0\langle\cos\theta\rangle = n_0\left(1-\frac{\text{NA}^2}{4m^2}\right) = n_0(1-\epsilon), \tag{D1}$$

where we define the dimensionless parameter $\epsilon = \text{NA}^2/4m^2$. This parameter directly quantifies the deviation from the paraxial regime and determines the magnitude of systematic biases in the reconstructed optical parameters.

(2) *Modified TIE.* Under finite NA conditions, the standard TIE is modified by replacing n_0 with n_{eff} in the phase gradient term:

$$\frac{\partial I}{\partial z} = -\frac{1}{kn_{\text{eff}}}\nabla_\perp\cdot(I\nabla_\perp\phi) - 2\frac{\partial\alpha}{\partial z}I, \tag{D2}$$

where $kn_{\text{eff}} = kn_0(1-\epsilon)$. This modification leads to systematic biases in the reconstructed optical parameters, as detailed in the following error propagation analysis.

b. Error propagation analysis

Wenow analyze how the effective refractive index modification propagates through the TIE reconstruction process to produce systematic errors in each optical parameter. Starting from the modified TIE with n_{eff}, we derive the relative errors for the phase (ϕ), intensity derivatives ($\partial\alpha/\partial z$, $\partial\beta/\partial z$), and the final reconstructed quantities: refractive index fluctuations (Δn), attenuation coefficient (μ), and attenuation asymmetry ($\mathcal{A}_\kappa$).

(1) *Phase recovery (ϕ).* The phase recovered from TIE inversion exhibits a systematic bias. When solving the modified TIE with n_{eff} instead of n_0, the reconstructed phase gradient is amplified by the factor $1/(1-\epsilon)$ due to the reduced effective refractive index in the denominator of the phase term. This leads to

$$\phi_{\text{measured}} = \frac{\phi_{\text{true}}}{1-\epsilon}. \tag{D3}$$

Relative error: $\delta_\phi = \epsilon/(1-\epsilon)$.

(2) *Intensity attenuation derivative ($\partial\alpha/\partial z$).* The intensity reduction parameter, extracted from symmetric intensity differences according to Eq. (7) in the main text, is independent of the effective refractive index to first order. This is because the phase contributions cancel in the symmetric combination $(I_+ + I_-)$, leaving only the intensity attenuation effect. The NA effect enters only through higher-order corrections related to the spatial extent of the intensity distribution:

$$\delta_{\partial\alpha/\partial z} \approx \mathcal{O}(\epsilon^2) \approx 0. \tag{D4}$$

(3) *Phase-coupling derivative ($\partial\beta/\partial z$).* The phase-coupling parameter is obtained from the transport of intensity equation through antisymmetric intensity differences. Since it is directly proportional to the phase gradient, and the phase gradient is amplified by the same factor $1/(1-\epsilon)$ as the phase itself due to the modified wave number in the TIE solution, it exhibits the same relative error:

$$\delta_{\partial\beta/\partial z} = \frac{\epsilon}{1-\epsilon}. \tag{D5}$$

(4) *Refractive index fluctuations (Δn).* From the reconstruction formula in the main text Eq. (8), refractive index fluctuations are computed from the ratio of phase-coupling and intensity derivatives. Since $\partial_z\beta$ is amplified by $1/(1-\epsilon)$ while $\partial_z\alpha$ remains unchanged, and the effective refractive index appears in both numerator and denominator of Eq. (D8), the combined effect after careful algebraic manipulation yields an amplification by $1/(1-\epsilon)^2$. For small ϵ, Taylor expansion gives

$$\Delta n_{\text{measured}} \approx \Delta n_{\text{true}}(1+2\epsilon+3\epsilon^2+\cdots). \tag{D6}$$

First-order relative error: $\delta_{\Delta n} \approx 2\epsilon = \text{NA}^2/(2m^2)$.

TABLE III. *Error estimations of attenuation coefficient (μ).* Systematic errors in μ remain negligible across all NA configurations due to operation in the transparent limit ($\Delta n < 1$). The $-2\epsilon\Delta n$ correction term ensures that attenuation measurements are inherently robust against NA-induced artifacts.

System	Measured μ (m^{-1})	Statistical RMS	Relative error	Systematic shift (m^{-1})	$\sigma_{\text{syst}}/\sigma_{\text{stat}}$
MLA	33.0	±27.3	−0.0135%	−0.004456	0.000163
HeLa	1300.4	±1905.2	−0.0415%	−0.539467	0.000283
Cell membrane	17012.6	±14258.0	−1.4340%	−244.037	0.017118

TABLE IV. *Error estimations of attenuation asymmetry ($\mathcal{A}_\kappa$).* The attenuation asymmetry exhibits strong robustness against NA effects, with systematic errors 1–3 orders of magnitude below statistical uncertainties. This exceptional stability validates the use of $\mathcal{A}_\kappa$ for testing optical reciprocity in heterogeneous media.

System	Measured A_κ	Statistical RMS	Systematic shift	$\sigma_{\text{syst}}/\sigma_{\text{stat}}$
MLA	0.024188	±0.424000	0.001225	0.002889
HeLa	0.057873	±0.301000	0.011783	0.039148
Cell membrane	−0.127788	±0.442000	−0.030899	0.069907

(5) *Attenuation coefficient (μ).* The attenuation coefficient, given by Eq. (9) in the main text, is the ratio of $\partial_z\alpha$ to $(1+\Delta n)$. Since $\partial_z\alpha$ is unaffected by NA to first order while Δn is overestimated by a factor $(1+2\epsilon)$, the denominator increases, leading to an underestimation of μ. The relative error becomes

$$\mu_{\text{measured}} \approx \mu_{\text{true}}(1-2\epsilon\,\Delta n). \tag{D7}$$

Relative error: $\delta_\mu \approx -2\epsilon\,\Delta n = -\text{NA}^2\Delta n/(2m^2)$.

Notably, in the transparent limit where $\Delta n < 1$, this systematic error becomes negligible.

(6) *Attenuation asymmetry ($\mathcal{A}_\kappa$).* The asymmetry parameter quantifies the breaking of optical reciprocity in heterogeneous media, as defined in Eq. (12) of the main text in terms of forward and backward propagation probabilities $\mathcal{P}(\pm\kappa)$, where $\kappa = \mu/(kn)$ is the normalized attenuation index.

For a wave propagating through a medium with both refractive index fluctuations (Δn) and attenuation (μ), the complex refractive index is $n = n_0(1+\Delta n + i\kappa)$. The transmission probability through a distance Δz involves both phase accumulation and amplitude decay. After propagating forward ($+z$ direction) and backward ($-z$ direction), the differential phase-amplitude coupling leads to

$$\mathcal{P}(\pm\kappa) = \exp(-2\mu\,\Delta z)\exp(\mp 2kn_0\Delta n\kappa\,\Delta z). \tag{D8}$$

Substituting these expressions into the asymmetry definition from Eq. (12) and simplifying the exponential terms, we obtain

$$\mathcal{A}_\kappa = -\tanh(2kn_0\Delta n\kappa\,\Delta z). \tag{D9}$$

This hyperbolic tangent form emerges naturally from the ratio of exponential differences, ensuring that $\mathcal{A}_\kappa$ is bounded between -1 and 1. The asymmetry vanishes for homogeneous media ($\Delta n = 0$) where reciprocity is preserved and provides a sensitive measure of reciprocity breaking in heterogeneous samples. The NA effect modifies the argument $\xi = 2kn_0\Delta n\kappa\,\Delta z$ through the following multiple pathways.(1) Effective wave number: $kn_0 \to kn_{\text{eff}} = kn_0(1-\epsilon)$; (2) biased Δn: $\Delta n_{\text{measured}} = \Delta n_{\text{true}}(1+2\epsilon)$; (3) modified κ through both μ and n_{eff}.

For small arguments ($|\xi| \ll 1$), the tanh function linearizes to $\tanh(\xi) \approx \xi$ and the combined NA effects result in a relative error:

$$\delta_{A_\kappa} \approx \epsilon = \frac{\text{NA}^2}{4m^2}. \tag{D10}$$

c. Quantitative error estimates for experimental systems

We apply the error propagation formulas derived above to quantify systematic uncertainties for our three experimental configurations: microlens array (MLA) with NA = 0.45, HeLa cells with NA = 1.20, and cell membrane with NA = 1.49. The systematic bias for each parameter is calculated by multiplying the measured value by the corresponding relative error formula: for Δn, the bias is $\Delta n_{\text{measured}}[1/(1-\epsilon)^2 - 1]$, for μ, it is $\mu_{\text{measured}}(-2\epsilon\,\Delta n)$, and, for $\mathcal{A}_\kappa$, it is approximately $\mathcal{A}_\kappa^{\text{measured}}\epsilon$ for small arguments. Tables I–IV present the calculated systematic shifts alongside measured statistical uncertainties, enabling direct comparison of their relative magnitudes.

The quantitative analysis reveals three distinct behaviors of NA-induced systematic errors across the optical parameters. As shown in Table I, the dimensionless parameter ϵ ranges from 0.022 for the MLA system to 0.242 for the cell membrane imaging. For refractive index fluctuations (Table II), systematic errors scale quadratically with NA^2/m^2, increasing from 4.5% for NA = 0.45 to 74% for NA = 1.49, and become comparable to statistical uncertainties at high NA ($\sigma_{\text{syst}}/\sigma_{\text{stat}} = 0.992$ for the oil-immersion objective). The attenuation coefficient (Table III) shows minimal sensitivity to NA effects, with relative errors remaining below 1.5% even at the highest NA, a consequence of the $-2\epsilon\,\Delta n$ correction term vanishing in the transparent limit where $\Delta n < 1$. The attenuation asymmetry (Table IV) demonstrates the strongest robustness, with systematic errors 6–9 orders of magnitude smaller than the measured values across all configurations. This substantial suppression of systematic errors in $\mathcal{A}_\kappa$ arises from the cancellation of attenuation contributions in the asymmetry ratio, leaving only a small residual effect from the phase-attenuation coupling. These findings confirm that while NA effects significantly impact phase-based measurements at high NA, reciprocity measurements through $\mathcal{A}_\kappa$ remain fundamentally insensitive to instrumentation artifacts, validating the reliability of our reciprocity invariance observations.

[1] M. R. Teague, Deterministic phase retrieval: A Green's function solution, J. Opt. Soc. Am. **73**, 1434 (1983).

[2] M. R. Teague, Irradiance moments: Their propagation and use for unique retrieval of phase, J. Opt. Soc. Am. **72**, 1199 (1982).

[3] N. C. Ruppel and M. A. Model, A guide to transport-of-intensity equation (TIE) imaging for biologists, Prog. Biophys. Mol. Biol. **198**, 1 (2025).

[4] N. Yoneda, J. Sakamoto, T. Tomoi, T. Nemoto, Y. Tamada, and O. Matoba, Transport-of-intensity phase imaging using commercially available confocal microscope, J. Biomed. Opt. **29**, 116002 (2024).

[5] C. Zuo, J. Li, J. Sun, Y. Fan, J. Zhang, L. Lu, R. Zhang, B. Wang, L. Huang, and Q. Chen, Transport of intensity equation: A tutorial, Opt. Lasers Eng. **135**, 106187 (2020).

[6] J. Li, N. Zhou, J. Sun, S. Zhou, Z. Bai, L. Lu, Q. Chen, and C. Zuo, Transport of intensity diffraction tomography with non-interferometric synthetic aperture for three-dimensional label-free microscopy, Light: Sci. Appl. **11**, 154 (2022).

[7] M. H. Jenkins and T. K. Gaylord, Three-dimensional quantitative phase imaging via tomographic deconvolution phase microscopy, Appl. Opt. **54**, 9213 (2015).

[8] Z. Bai, Q. Chen, H. Ullah, L. Lu, N. Zhou, S. Zhou, J. Li, and C. Zuo, Absorption and phase decoupling in transport of intensity diffraction tomography, Opt. Lasers Eng. **156**, 107082 (2022).

[9] E. Wolf, Three-dimensional structure determination of semi-transparent objects from holographic data, Opt. Commun. **1**, 153 (1969).

[10] R. J. Potton, Reciprocity in optics, Rep. Prog. Phys. **67**, 717 (2004).

[11] M. Watabe, Y. Hirano, A. Iwane, O. Matoba, and K. Takahashi, Optical dispersions through intracellular inhomogeneities, Phys. Rev. Res. **5**, L022043 (2023).

[12] S. Mazumder, *Numerical Methods for Partial Differential Equations: Finite Difference and Finite Volume Methods*, 1st ed. (Academic Press, New York, 2016).

[13] B. Xue and S. Zheng, Phase retrieval using the transport of intensity equation solved by the FMG-CG method, Optik (Stuttgart, Ger.) **122**, 2101 (2011).

[14] S. V. Pinhasi, R. Alimi, L. Perelmutter, and S. Eliezer, Topography retrieval using different solutions of the transport intensity equation, J. Opt. Soc. Am. A **27**, 2285 (2010).

[15] W. H. Press, S. A. Teukolsky, W. T. Vetterling, and B. P. Flannery, *Numerical Recipes in C: The Art of Scientific Computing*, 2nd ed. (Cambridge University Press, Cambridge, UK, 1992).

[16] MLA300-14AR-M-$\phi 1''$ mounted lens array–Thorlabs, https://www.thorlabs.co.jp/thorproduct.cfm?partnumber=MLA300-14AR-M, accessed: 2025-05-01.

[17] Data is available at Zenodo, https://doi.org/10.5281/zenodo.15589385.

[18] M. Watabe, Physical constraints to phase retrieval using the transport of intensity equation in fluorescence microscopy imaging, presented at the *1st Conference for Sensing and Imaging Through Scattering and Fluctuating Field in Biology, Telecommunication and Astronomy (SI-Thru2022), April 19–22, 2022 at Pacifico Yokohama, Japan* (Optics & Photonics International Council, Tokyo, Japan, 2022).

[19] T. Yamada, H. Yoshimura, R. Shimada, M. Hattori, M. Eguchi, T. K. Fujiwara, A. Kusumi, and T. Ozawa, Spatiotemporal analysis with a genetically encoded fluorescent RNA probe reveals TERRA function around telomeres, Sci. Rep. **6**, 38910 (2016).

[20] Xenon arc light sources–Thorlabs, https://www.thorlabs.com/newgrouppage9.cfm?objectgroup_ID=13016, accessed: 2025-04-10.